Insights into Imaging

CRITICAL REVIEW

Open Access

Multi-nuclear magnetic resonance spectroscopy: state of the art and future directions

Yi Wei[1†], Caiwei Yang[1†], Hanyu Jiang[1], Qian Li[1], Feng Che[1], Shang Wan[1], Shan Yao[1], Feifei Gao[1], Tong Zhang[1], Jiazheng Wang[2] and Bin Song[1,3*]

Abstract

With the development of heteronuclear fluorine, sodium, phosphorus, and other probes and imaging technologies as well as the optimization of magnetic resonance imaging (MRI) equipment and sequences, multi-nuclear magnetic resonance (multi-NMR) has enabled localize molecular activities in vivo that are central to a variety of diseases, including cardiovascular disease, neurodegenerative pathologies, metabolic diseases, kidney, and tumor, to shift from the traditional morphological imaging to the molecular imaging, precision diagnosis, and treatment mode. However, due to the low natural abundance and low gyromagnetic ratios, the clinical application of multi-NMR has been hampered. Several techniques have been developed to amplify the NMR sensitivity such as the dynamic nuclear polarization, spin-exchange optical pumping, and brute-force polarization. Meanwhile, a wide range of nuclei can be hyperpolarized, such as ^{2}H, ^{3}He, ^{13}C, ^{15} N, ^{31}P, and ^{129}Xe. The signal can be increased and allows real-time observation of biological perfusion, metabolite transport, and metabolic reactions in vivo, overcoming the disadvantages of conventional magnetic resonance of low sensitivity. HP-NMR imaging of different nuclear substrates provides a unique opportunity and invention to map the metabolic changes in various organs without invasive procedures. This review aims to focus on the recent applications of multi-NMR technology not only in a range of preliminary animal experiments but also in various disease spectrum in human. Furthermore, we will discuss the future challenges and opportunities of this multi-NMR from a clinical perspective, in the hope of truly bridging the gap between cutting-edge molecular biology and clinical applications.

Keywords: Hyperpolarization, Multi-nuclear magnetic resonance, Magnetic resonance spectroscopic imaging, Clinical application

Key points

- The multi-NMR by HP has been applied in many diseases. It has allowed for real-time assessment of human metabolism in vivo and can promote a shift from morphological to molecular level.
- Work is ongoing in clinical translation of multi-NMR, with numerous spectrum of human diseases, and bridging the gap between the molecular level imaging and clinical applications will foster and introduce future opportunities in this field.

Background

Since 1938, the phenomenon of NMR discovered by Rabi when sent a beam of molecules through magnetic field and found that they could be made to emit radio waves at

†Yi Wei and Caiwei Yang these authors have contributed equally to this work.

*Correspondence: songlab_radiology@163.com

[1] Department of Radiology, West China Hospital, Sichuan University, No. 37, Guoxue Alley, Chengdu 610041, People's Republic of China
Full list of author information is available at the end of the article

specific frequencies, great advances in the research and clinical applications of magnetic resonance (MR) imaging have been obtained and leaved remarkable contributions in human health [1]. At present, the development of medical imaging is not only confined to observation of lesions from morphological changes, but also toward a more in-depth comprehensive assessment of biological behavior, pathophysiological, and metabolic changes, and thus to achieve a more precise personalized medicine. With the development of MR hardware (magnets, gradients, radiofrequency coils) and software (pulse sequences, data reconstruction algorithms), the clinical application of multi-nuclear magnetic resonance spectroscopy provides the possibility of real-time dynamic visualization of the metabolic changes and specific substrate to metabolic conversion of the lesion in vivo, which also pushes the MR imaging into a more in-depth molecular level [2].

In theory, any nucleus that can be detected by NMR can be imaged with MR imaging. ^{1}H is the mostly used atom because of the high concentration in human body and large value of the gyromagnetic ratio which enables to achieve high-resolution T1- or T2-weighted MR images. However, the complicated background signal, signal overlaps, and the ability to only reflect a few molecules such as such as choline, creatine, NAA, glycine, myo-inositol, lactate, alanine, and acetate for ^{1}H also limit its application in the real-time metabolic activity. Using of higher magnetic fields, developing of new detectors, increasing the signal with hyperpolarization, and obtaining the signal with ultra-fast pulse sequences make the other nucleus imaging spectroscopy like ^{2}H, ^{13}C, ^{15} N, ^{18}F, ^{23}Na, ^{31}P, and ^{129}Xe come true [3–5]. These multi-NMR spectroscopies provide the ability to insight the multiple metabolic activities and reflect the real metabolism in vivo and have the potential to really bridge the gap between the cutting-edge molecular biology, biochemistry, and metabolism research.

In this review, we will provide an overview of the clinical application of multi-nuclear magnetic resonance spectroscopy in the various biologic processes with different lesions. In addition, we will also discuss the future challenges and opportunities of this novel imaging technique from a clinical perspective, hoping to real bridge the gap between the cutting-edge molecular biology and clinical applications.

Nervous system

Metabolic abnormalities are key factors in many neurological disorders. The ability to accurately measure this metabolic damage could improve the detection and diagnosis of disease progression and facilitate the development of new treatments accordingly. Hyperpolarized (HP)-carbon-13 magnetic resonance spectroscopic imaging (MRSI) is an emerging imaging technique that allows the noninvasive, real-time measurement of enzyme activity in living organisms (Fig. 1). To date, this metabolic imaging method has been used mainly in the fields of cancer and cardiology and has recently begun to be used to study neurological diseases [6, 7]. HP-^{13}C MRSI has promising applications in neurodegenerative diseases, traumatic brain injury, stroke, and brain tumors [8].

Neurodegenerative diseases

Mononuclear phagocytes (MPs) play a crucial role in the progression of multiple sclerosis (MS) and other neurodegenerative diseases [9–11]. Following activation and subsequent differentiation toward a proinflammatory phenotype, abnormalities in MPs metabolism occur, leading to increased glycolysis and lactate production. HP-^{13}C MRSI is a clinically translatable imaging modality that allows for the noninvasive detection of metabolic pathways in real time. ^{13}C MRSI not only tracks the Warburg effect within the tumor but also allows for a realistic neurological inflammatory response. The significant increase in HP-[1-^{13}C]-pyruvate to HP-[1-^{13}C]-lactate conversion, on the one hand, indicated the presence of a high density of proinflammatory MPs. On the other hand, it suggested that the increase in HP-[1-^{13}C]-lactate may be mediated by upregulation of pyruvate dehydrogenase (PDH) kinase-1 in activated MPs leading to regional PDH inhibition [12]. Overall, the preclinical results of the cuprizone model demonstrated the potential of ^{13}C MRSI of HP-[1-^{13}C]-pyruvate as a neuroimaging method for the assessment of inflammatory lesions. This method could prove useful not only for multiple sclerosis, but also for other neurological disorders with an inflammatory component in the future.

Traumatic disease

Traumatic brain injury (TBI) can lead to disturbances in energetic metabolism in the brain but monitoring of metabolic activity is currently achieved mainly by microdialysis and ^{18}F-fluorodeoxyglucose (^{18}F-FDG) positron emission tomography (PET) [13]. Proton magnetic resonance spectroscopy (^{1}H MRS) also detected focal or systemic elevated lactate and related PDH caused by primary or secondary injured inflammation [14, 15]. HP-^{13}C MRSI could be used as a direct, rapid, and noninvasive method to explore the effects of TBI on energetic metabolism in the brain [16, 17]. In rats with moderate TBI induced by control cortical impingement on one cerebral hemisphere, measured by injection of HP-[1-^{13}C]-pyruvate, the injured side of the brain was found to produce a ^{13}C-bicarbonate signal 24 ± 6% lower than the injured side, while the HP-bicarbonate-to-HP-lactate ratio was

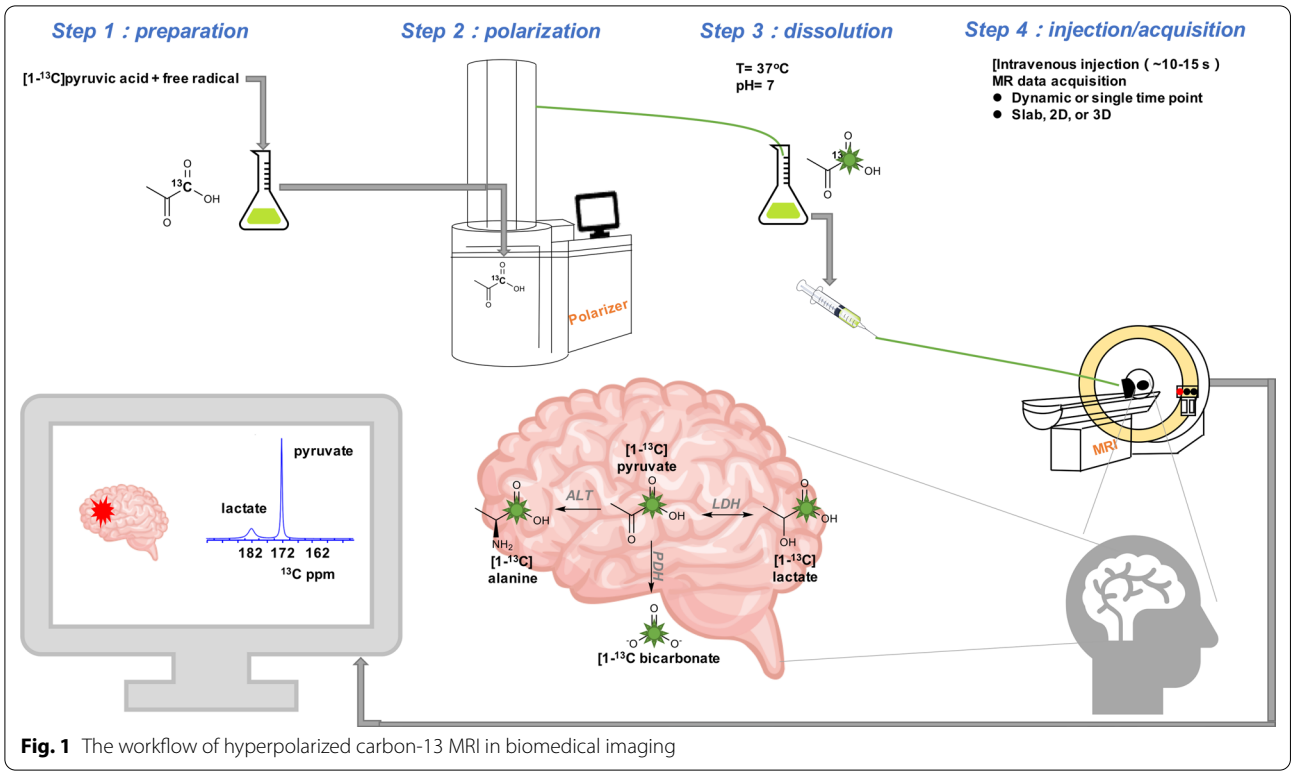

Fig. 1 The workflow of hyperpolarized carbon-13 MRI in biomedical imaging

33 ± 8% lower than that of the injured side [16]. In controls, there were no significant differences in signals between the two cerebral sides. The results suggest that mitochondrial pyruvate metabolism is impaired, resulting in reduced aerobic respiration at the injury site after TBI. Clinically, HP-[1-^{13}C]-pyruvate MRSI is used to image patients with acute mild TBI several days after head trauma, but with no obvious anatomic changes. One patient showed high levels of lactic acid production at the injured site, and both patients showed a notable reduction in bicarbonate production [17] (Fig. 2). This study indicates using HP-pyruvate feasibly to image the metabolic changes in TBI patients and proves the transformability and sensitivity of this technology to the changes in cerebral metabolism after mild TBI.

Stroke

Ischemic stroke is a progressive process characterized by impaired but reversible damage to the metabolic activity of the penumbra tissue so that if blood flow is restored, full recovery of function is possible. Currently, ischemic cases are identified by a mismatched area between perfusion and diffusion on MRI. Conventional perfusion and diffusion proton MR images have a large background signal, and the commonly used contrast injection is an invasive method, but many patients with the renal injury cannot use contrast agents and results have shown that gadolinium contrast agents can cause nephrogenic systemic fibrosclerosis. Due to the high rate of glucose extraction in the penumbra, characterized by anaerobic glycolysis and subsequent increased lactate production, this can be detected by the altered metabolism of HP-^{13}C-pyruvate. HP-^{13}C MRI may therefore have an important role in understanding the development and response of the ischemic putative difficult zone in stroke and is also translatable to concurrent studies of metabolism and perfusion in humans [18] (Fig. 3). In preclinical trials, an endothelin-1-induced ischemic stroke model was used to assess metabolic alterations after acute ischemic stroke in rats [19]. The results showed increased total lactate production in the ischemic hemispheric dark zone compared to the contralateral brain. This was the result of a combination of increased pyruvate in the blood and lactate dehydrogenase (LDH)-mediated lactate production. When estimating penumbra viability, measures of penumbra metabolic activity may be more sensitive than conventional imaging techniques. Likewise, since the ^{129}Xe signal is proportional to cerebral blood flow as a perfusion missing agent for cerebral blood flow, HP-^{129}Xe MRI can also be used for the study of ischemic semi-dark areas as a perfusion missing agent of cerebral blood flow. The high lipid solubility, lack of biological tissue background signals, and high sensitivity of HP-^{129}Xe allow the detection of HP-^{129}Xe signals even at low concentrations,

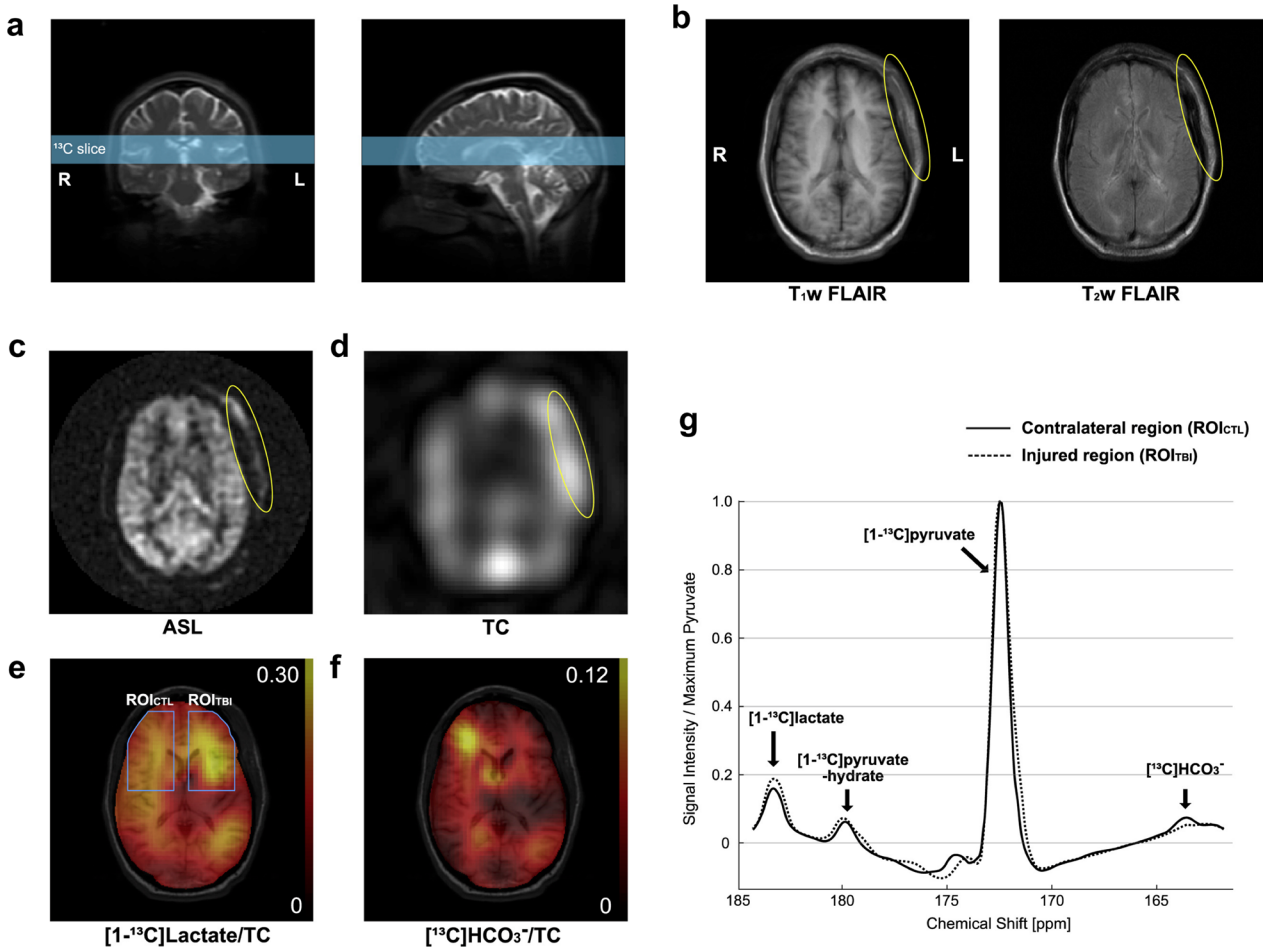

Fig. 2 Metabolism of acute traumatic brain injury (TBI) imaged by hyperpolarized 13C-pyruvate. The patient (35 years old, male), injured on the left frontal scalp, was imaged 28 h after the injury. **a** An axial slice that includes the injured region was prescribed for 13C imaging. **b** T1-weighted and T2-weighted 1 H FLAIR and (**c**) ASL images showed swelling and increased perfusion in the injured site outside the skull (yellow circle), whereas no cerebral contusion, hemorrhage or hypoperfusion were detected. **d** Region with increased total hyperpolarized 13C signal image matched to the scalp edema. **e** Increased [1-13C]lactate conversion and (**f**) decreased [13C]HCO3 – production were detected in the brain tissues of the injured hemisphere. **g** Averaged spectra over the injured brain region and the contralateral normal-appearing brain region. Reproduced with permission from Elsevier Ltd (License Number: 5324100264979). iScience. 2020 Nov 30;23(12):101,885

which is advantageous for the identification of underperfused brain tissue. Using HP-^{129}Xe MRI, Zhou et al. [20] successfully detected a local decrease in cerebral blood flow and studied ischemic lesions in the core of stroke by performing a permanent middle cerebral artery occlusion on the right brain of rats. This demonstrated that HP-^{129}Xe MRI can be used as a complementary tool to conventional MRI to study the pathophysiology of cerebral under perfusion.

Brain tumor

The current "open questions" in neuro-oncology imaging are to evaluate tumor response during and after treatment on clinically relevant timescales, to differentiate between recurrent or residual tumors and treatment-related changes with high specificity, to classify tumor pathological aberrations at the molecular level, and to predict tumor response to treatment. Metabolic biomarkers could potentially address these issues and could in principle monitor response before genetic alterations or more delayed morphological changes or recurrence.

Hydrogen is the basic building block of biological organic molecule, and therefore, deuterium (hydrogen 2 (^{2}H)) is characterized by nondestructive labeling, labeling flexibility, and potential adaptability. At present, in the early stages of research, animal studies have shown that ^{2}H MRSI and MRI can be used to quantify ^{2}H-labeled glucose metabolism in tumors [21–23].

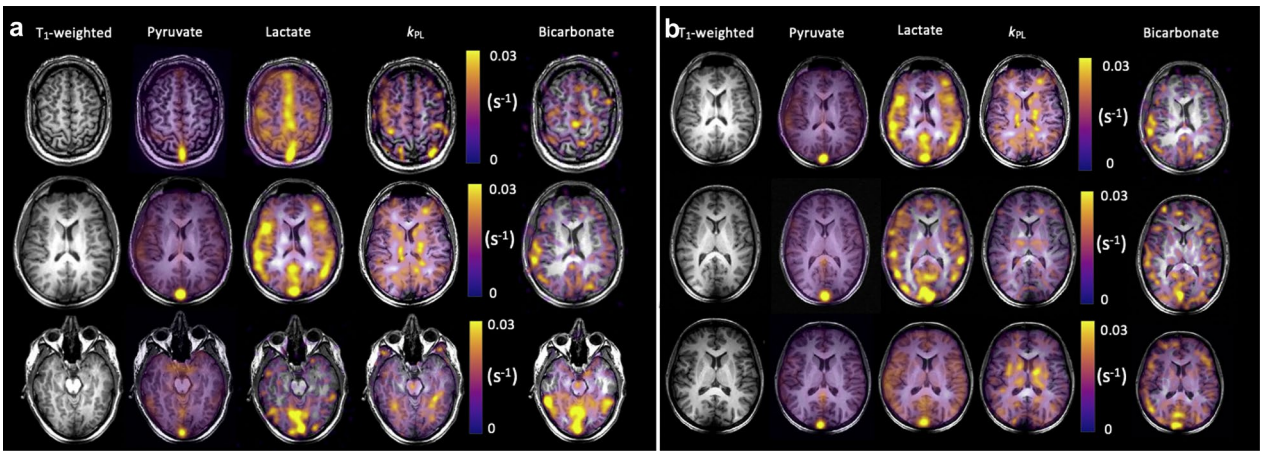

Fig. 3 Iterative Decomposition with Echo Asymmetry and Least squares estimation (IDEAL) spiral 13C imaging demonstrating metabolite distribution in the healthy human brain. NeuroImage Volume 189, 1 April 2019, Pages 171–179

HP-[1-^{13}C]-pyruvate MRI is a novel method for demonstrating energetic metabolism in the human brain and brain tumors, in contrast to the clinical needs that cannot be met by current conventional imaging techniques [24–28] (Fig. 4). HP-pyruvate MRSI was a valuable tool for monitoring the phosphatidylinositol 3-kinase

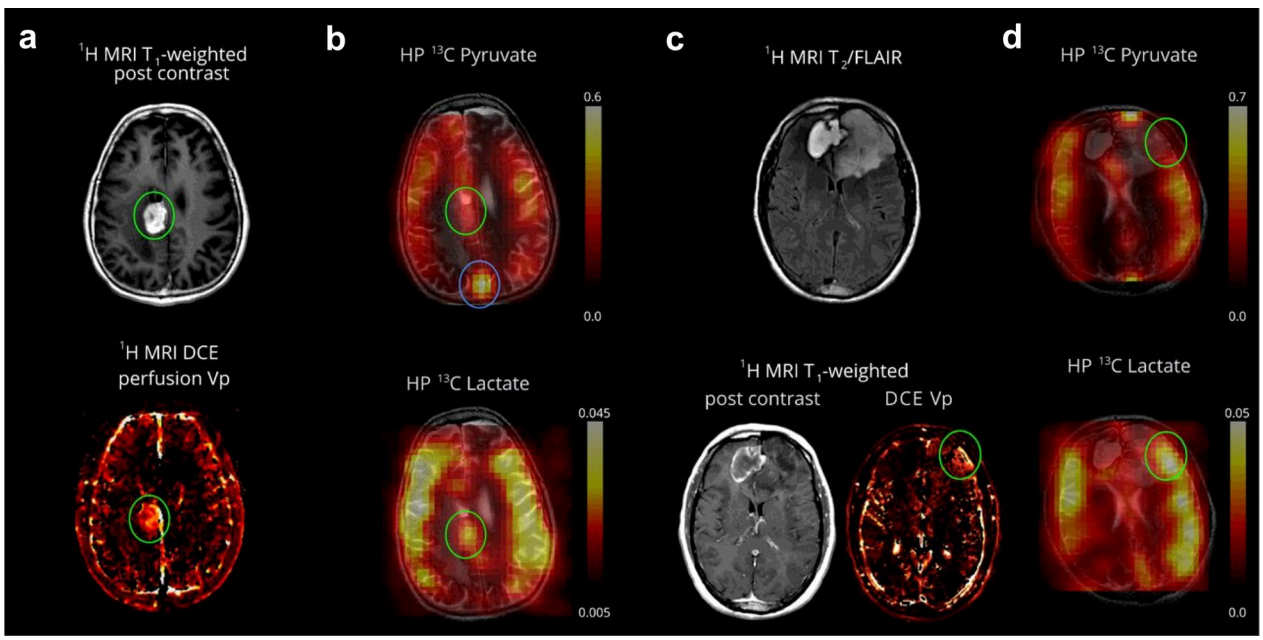

Fig. 4 Pyruvate metabolism in a recurrent glioblastoma and treatment-related changes (Patient 2, a and b) and anaplastic oligodendroglioma (Patient 1, c and d). An enhancing mass is located in the right cingulate gyrus (green oval) (**a**). The hyperpolarized pyruvate map shows high signal corresponding to the cortex/juxtacortical regions and superior sagittal sinus. The volume normalized pyruvate signal in the lesion is 1.3-fold higher than the entire brain. The HP lactate map shows mildly elevated signal corresponding to the lesion, similar to background lactate production by the brain. The volume normalized lactate signal in the lesion is 1.0-fold of the lactate over the entire brain (cortex and white matter) (**b**). The T2-FLAIR image shows an expansile left frontal mass and contracting right frontal hematoma. The left frontal mass has minimal, patchy enhancement and a small component of elevated plasma volume (green oval) visualized by DCE MRI (**c**). The HP pyruvate map shows high signal corresponding to the cortex/juxtacortical regions and superior sagittal sinus, but relatively lower signal corresponding to the small hyperperfused component. The HP lactate map shows mildly elevated signal corresponding to the hyperperfused component, similar to background lactate production by the brain (**d**). Cancer Res. 2018;78(14):3755–3760

inhibitor LY294002 in mouse models of malignant glioma and breast cancer, where inhibition of the phosphatidylinositol 3-kinase pathway led to reduced LDH activity, thereby reducing the signal for HP conversion of pyruvate to lactate [29]. Park et al. also used HP-^{13}C-pyruvate MRSI to assess the prognosis of a rat glioma model [24]. The signal-to-noise ratio of ^{13}C-pyruvate and its metabolic^{13}C-lactate were both significantly higher than that of normal brain tissue, where the blood–brain barrier (BBB) was able to restrict the entry of pyruvate into brain cells, whereas the disruption of the BBB in gliomas resulted in the smooth entry of ^{13}C-pyruvate into brain tissue, which had lagged its research in oncology and cardiology. Nevertheless, Hurd et al. found that injections of [1-^{13}C]-ethyl pyruvate (a lipophilic pyruvate derivative) were able to cross the BBB faster than pyruvate and had a significantly higher polarization ratio than total carbon in brain tissue [25], opening a new direction for HP MRSI in the brain. In preliminary studies performed in patients with primary brain tumors, HP-[1-^{13}C]-pyruvate rapidly crossed the BBB and was converted to the metabolites lactate and bicarbonate. Non-tumor areas showed a high bicarbonate signal, while tumor areas had a low bicarbonate signal, suggesting that this technique may be valuable for exploring mitochondrial oxidative metabolism and its alterations in brain tumors [26]. Another recent study similarly formalized the feasibility of obtaining high-quality metabolite maps in patients with primary or metastatic brain tumors [27]. These initial clinical studies demonstrate the feasibility of HP-[1-^{13}C]-pyruvate MRI for cerebral metabolism assessment.

Genitourinary system disease

Tumors

In prostate cancer, antisense oligonucleotides targeting monocarboxylate transporter (MCT)-4 that inhibit lactate secretion may be useful in treating castration-resistant prostate cancer and other cancers because they can interfere with the reprogrammed energetic metabolism of cancer, an emerging hallmark of cancer [30]. Recent preclinical experiments demonstrated that MCT1 regulated pyruvate transport into the cell, MCT4 regulated lactate transport outside the cell body and MCT1 expression had a strong positive correlation with Gleason grade of prostate cancer [31]. Similarly, Keshari et al. used the HP-^{13}C-pyruvate co-reactor to study renal cancer cells and found that metabolic pathways could be observed in real time and that changes in the microenvironment caused by oxidation, flux, pH, and substrate could be controlled, revealing the importance of MCT4 transport in disease onset and progression and that MCT4-mediated regulation of lactate transport could be detected by HP-^{13}C MRSI [32]. Sriram et al. found that in malignant cells, MCT4 transport of lactate to the extracellular compartment was increased, so the ratio of intracellular to extracellular lactate predicted the aggressiveness of tumor cells [33]. Another research confirmed by HP-^{13}C-pyruvate metabolism in in vivo renal tumor tissue that, compared with benign renal tumors, approximately 70–80% of renal cell carcinomas (RCC) had increased lactate production and extracellular translocation was increased, and its aberrant metabolism was mainly caused by increased expression of LDHA and MCT4 [34]. Therefore, benign renal tumors can be differentiated from RCC by assessing the rate of HP-[1-^{13}C]-pyruvate-to-lactate conversion and extracellular transport of lactate. In addition, HP-[1-^{13}C]-pyruvate MRI can noninvasively assess the aggressiveness of RCC. Sriram et al. [35] found that the expression of LDHA-catalyzed conversion of pyruvate to lactate varied among tumor lines, and HP- [1-^{13}C]-pyruvate MRI and diffusion-weighted imaging were used to differentiate between benign renal tumors and renal cell carcinomas by tumor [1-^{13}C]-pyruvate conversion rate, LDHA expression rate, and [1-^{13}C]-lactate apparent diffusion coefficient values to assess the aggressiveness of renal tumors and to guide the corresponding clinical treatment.

The first clinical trials of HP-[1-^{13}C]-pyruvate MRI and MRSI were successfully used in prostate cancer patients [36]. Recently, Sushentsev N et al. [37] also found that HP 13C-MRI can noninvasively differentiate indolent from aggressive prostate tumors based on their characteristic metabolic features (Fig. 5). Preclinical studies have shown that elevated [1-^{13}C]-lactate is observed in animal models of prostate cancer and that the [1-^{13}C]-lactate-to-[1-^{13}C]-pyruvate ratio at the cancer site increased with increasing cancer stage; this ratio decreased with effective treatment [38–40]. This clinical trial study firstly demonstrated that HP-[1-^{13}C]-pyruvate MRSI could be used safely and effectively in humans and secondly observed a significant [1-^{13}C]-lactate peak and an increase in the [1-^{13}C]-lactate-to-[1-^{13}C]-pyruvate ratio in the lesion, while healthy prostate tissue and surrounding vascular tissue showed no or very low [1-^{13}C]-lactate peaks [36]. This result is consistent with the results of preclinical experimental studies [38]. Albers et al. performed HP-[1-^{13}C]-pyruvate MRSI in a transgenic mouse model of prostate cancer and found significant differences in the lactate content of highly differentiated prostate cancer, poorly differentiated prostate cancer, normal tissue surrounding the prostate, and metastatic lymph nodes [38]. Another noteworthy finding is that in a patient with biopsy-confirmed bilateral prostate cancer foci, conventional T2-weighted image, ADC image, and ^{1}H MRSI on staging showed lesions only on the right side of the gland, while [1-^{13}C]-pyruvate MRSI

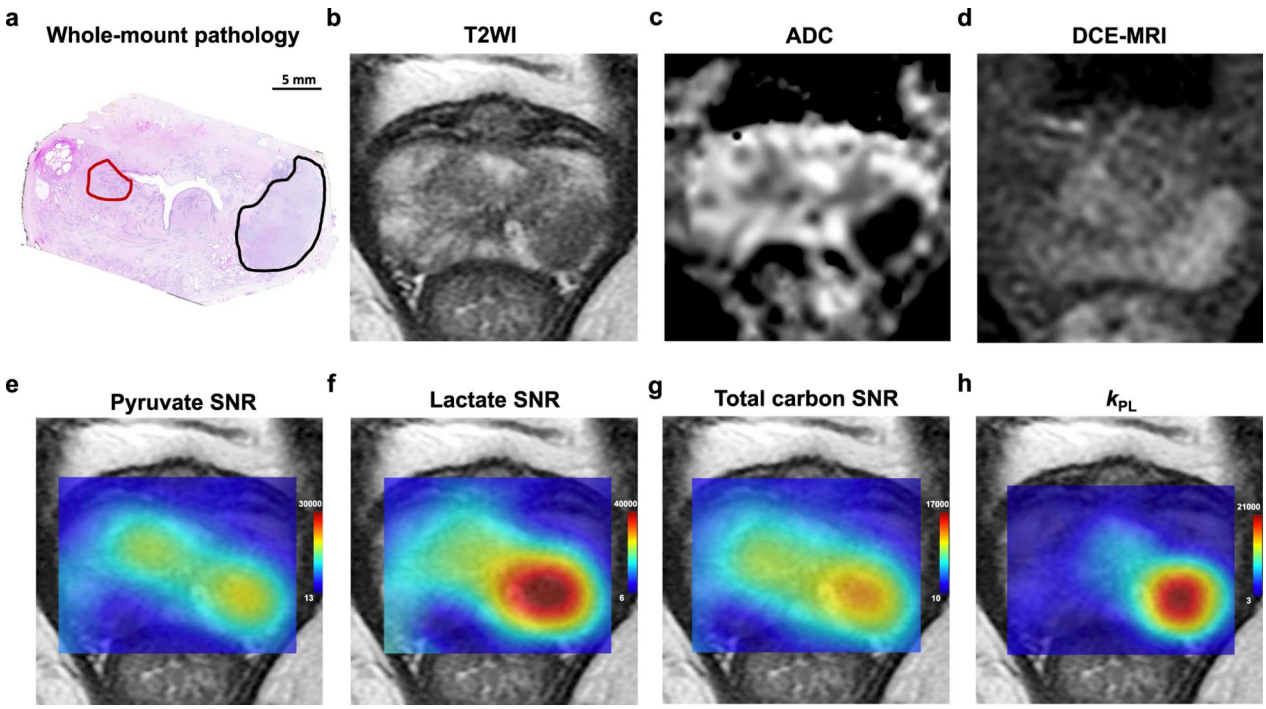

Fig. 5 Representative example of an MR-occult transition zone tumor detected on hyperpolarized 13C-MRI. **a** Post-surgical histopathological assessment confirmed the diagnosis of multifocal adenocarcinoma of the prostate. An International Society of Urological Pathology (ISUP) grade 3 target lesion was visible on 1H-MRI in the left peripheral zone: Prostate Imaging-Reporting and Data System (PI-RADS) 5 target lesion; black region of interest (ROI). **b** Standard-of-care T2-weighted MRI demonstrating a marked area of low signal intensity corresponding to the target lesion in the left peripheral zone. **c** ADC map demonstrating a corresponding focus of markedly restricted diffusion in the left peripheral zone. **d** Dynamic contrast-enhanced (DCE) MRI demonstrating the area of early enhancement in the left peripheral zone. **e** Pyruvate signal-to-noise ratio (SNR) map with two areas of high pyruvate signal, both corresponding to histopathology-confirmed tumor foci. **f** Lactate SNR map demonstrating high [1-13C] lactate signal in the grade 3 left peripheral zone lesion. **g** Total carbon SNR map showing higher signal in the left peripheral zone tumor. **h** K_{pl} map (presented as s − 1) showing a higher rate of pyruvate-to-lactate conversion in the more aggressive left peripheral zone lesion. Nat Commun. 2022 Jan 24;13(1):466

monitored areas of high [1-^{13}C]-lactate-to-[1-^{13}C]-pyruvate signal ratio on both the left and right sides of the gland, which was later confirmed by MR guided re-biopsy that confirmed a bilateral cancer focus [36]. This heralds the value of [1-^{13}C]-pyruvate metabolic imaging for noninvasive tumor diagnosis, demonstrating that metabolic changes precede changes in MRI signal. In addition, the surprising finding that HP-[1-^{13}C]-pyruvate MRSI can detect bilateral cancers may become a particularly important monitoring tool for patients in the slow-growing cancer category. Furthermore, for assessing tumor response to treatment, HP-[1-^{13}C]-pyruvate MRSI could detect reduced pyruvate–lactate conversion early after treatment of prostate cancer [41], though low uptake and high background uptake in primary prostate cancer tissue when detected by ^{18}F-FDG PET uptake imaging modalities observe the metabolic response of cancer cells more difficult [42]. Therefore, HP-[1-^{13}C]-pyruvate MRSI has the potential to provide an early assessment of tumor treatment efficacy.

Other kidney lesions

Alport syndrome (AS) is a genetic disorder characterized by impaired renal function. The development of noninvasive tools for early diagnosis and monitoring of renal function during disease progression is of clinical importance. HP-^{13}C MRI is an emerging technology that allows noninvasive, real-time measurement of metabolism in vivo. A study investigated the feasibility of using this technique to assess changes in renal metabolism in a mouse model of AS. Mice with AS had significantly lower lactate levels from 4 to 7 weeks of age, whereas control mice had no change in lactate levels over time. The results of this study suggest that HP-^{13}C MRI may provide a potential noninvasive tool for characterizing disease progression in AS. Furthermore, HP-^{13}C MRSI was used for noninvasive assessment of oxidative stress and mitochondrial PDH activity after ischemia–reperfusion injury in the kidney. The changes in renal redox capacity and mitochondrial PDH activity on day 7 after injury in unilateral rat kidneys were observed by

HP-[1-^{13}C]-dehydroascorbate and^{13}C-pyruvate MRSI, respectively, and it was found that on day 7 of ischemia–reperfusion injury, renal ^{13}C-vitamin C-to-vitamin C plus dehydroascorbate ratio and ^{13}C-bicarbonate-to-^{13}C-pyruvate ratio were reduced, consistent with their low redox capacity, and PDH activity was impaired [43].

Liver diseases

Metabolic liver disease

A growing body of studies suggests that HP ^{13}C MRI is promising for assessing liver metabolism, diagnosing liver injury by mapping the dynamic conversion of HP ^{13}C substrate [44–47]. Evidences indicates that increased [1-13C]pyruvate-to-alanine-and-lactate conversion was observed in a model of chemically induced inflammatory liver injury, and the conversion of [1-13C]DHA-to-vitamin C was noted reduction in a diet-induced steatohepatitis model [2, 46, 48]. Jeong et al. found that the increased levels of alanine and lactate are useful biomarkers for fatty liver diseases. Merritt et al. studied the metabolism of HP [1-13C]pyruvate in tricarboxylic acid (TCA) cycle in rat livers and indicated that the major pathway for entry of HP [1-13C]pyruvate into the hepatic TCA cycle is via pyruvate carboxylase, and that cataplerotic flux through phosphoenolpyruvate carboxykinase (PERCK) is the primary source of [^{13}C]bicarbonate [44, 49]. Another study conducted by Emine et al. [50] also showed that [^{13}C]bicarbonate labeled from hyperpolarized [1- 13 C]pyruvate is an in vivo marker of hepatic gluconeogenesis in fasted state. Furthermore, the metabolic changes can be also quantified by HP ^{13}C [45, 51–53]. Smith et al. [54]. measured the time to peak (TTP) of HP ^{13}C-pyruvate and its metabolites in non-alcoholic fatty liver disease (NAFLD) and normal pigs, and their results revealed that the decreased liver lactate TTP in ^{13}C spectra in NAFLD pigs, indicating an increased rate of lactate production and a disturbance in liver lipid synthesis. These results suggested that HP ^{13}C can be used as a method for assessing in vivo hepatic metabolism and may have the potential to address a currently unmet clinical need for investigating mechanisms of fatty liver diseases (FLD), noninvasive evaluation of these pathways during the detection and treatment of FLD in general.

Hepatocellular carcinoma

Cancer development is a multi-step process involving genetic and cellular alterations, and the multi-step hemodynamic changes for HCC during hepatocarcinogenesis have been well documented [55]. The routine used diagnostic criteria mainly refers on the vascular criteria due to the angiogenesis or neovascularization and the portal flow diminishes. However, since HCC occurs mostly within the liver parenchyma in cirrhosis, its structure is heterogeneous and manifests as multiple mass-like nodules [56]. Thus, the detection of small or very early HCC can be extremely challenging with routine imaging modalities using the vascular criteria. Using HP ^{13}C MRI, Hu et al. [57] examined a model of Myc gene-induced liver cancer and found that changes in tumor metabolism precede all observable morphological and histological changes. In particularly, their results also showed that the conversion of pyruvate to alanine was significantly increased in precancerous tissue and which has become the highest alanine content region, whereas alanine was absent in healthy or established tumors. In addition to the application of early HCC detection, HP ^{13}C MRI is also useful for the assessment of the biological characteristics [58, 59]. Bliemsrieder et al. [60] presented an in vivo imaging technique for metabolic tumor phenotyping in rat models of HCC, and higher pyruvate-to-lactate conversion rates and lactate signal in subcutaneous tumors were derived from high lactate-to-alanine tumor cells and which may represent a higher biological aggressiveness. Thus, metabolic alterations detected by HP ^{13}C MRI provide more insights into tumor heterogeneous characteristics and therefore may act as a biological and prognostic biomarker for HCC.

Pulmonary diseases

Currently, imaging techniques commonly used in clinical practice for the diagnosis of lung diseases include chest X-ray and computed tomography, which can obtain structural information about the lung, but they are both radioactive and cannot obtain imaging information about the gas exchange function of the lung, while usually the occurrence and development of diseases undergo a process from functional to structural lesions. Therefore, there is an urgent need to develop a non-radioactive imaging technique to detect the gas exchange function of the lung, which can be used for the early study and diagnosis of major lung diseases. Noninvasive, non-radioactive MRI has been used to obtain images of most living organs and tissues, such as the brain, heart, and abdomen, and is widely used in in vivo imaging studies and clinical disease diagnosis. However, the conventional proton (^{1}H)-based MRI technique is not applicable to the lung because the lung tissue is mostly at the gas–solid interface, and thus, the magnetization rate varies greatly, resulting in a very short transverse relaxation time (T2) of protons, and even with ultrashort TE imaging sequences [61, 62], only partial information of the airways of the lung can be obtained. Moreover, the lung is composed of mostly cavernous structures, and the density of gas in the alveoli is about 1,000 times lower than that of ordinary tissues, and it is difficult to image the gas in the alveoli with conventional MRI techniques. To

achieve MRI of lung gases, it is necessary to increase the polarization of the gas and thus enhance the sensitivity of the MRI signal.

The noble gases (^{3}He or ^{129}Xe) nuclear spins are hyperpolarized, using the spin-exchange optical pumping (SEOP) technique, by several orders of magnitude compared to the Boltzmann population [63]. This leads to amplification of the MRI sensitivity by orders of magnitude compared to that of thermal equilibrium, enabling sensitive diagnosis of lung diseases by measuring associated changes in the lung's structure and function. ^{3}He and ^{129}Xe are presently the most used gases for HP-gas lung MRI (Fig. 6), and in recent years, HP-^{83}Kr and HP-^{19}F have also been reported in the literature for lung gas MRI studies [64–68]. HP-gas MRI could obtain lung images reflecting lung morphology and ventilation status, enabling visual detection of lung diseases [69–73], and HP-gas MRI could differentiate the severity of asthma [73] (Fig. 7). In combination with proton-based lung contour imaging, HP-gas MRI of lung structures can quantitatively study pulmonary ventilation disorders. Lange et al. used lung contour and ventilation information from HP-^{3}He MRI to calculate ventilation deficits in healthy volunteers and patients with different degrees of asthma, and their results were not only consistent with conventional respiratory volume measurements but also allowed differentiation of asthma severity [70]. It was also possible to detect ventilation deficits in smokers with normal lung function test [71]. Since then, researchers have developed a series of semi-automated and automated algorithms and have gradually moved toward HP-^{129}Xe MRI of the lungs [72] and have demonstrated that the use of HP-^{129}Xe MRI and semi-automated calculations can also differentiate between healthy volunteers and patients with chronic obstructive pulmonary disease patients (Fig. 8).

Using ultra-fast imaging sequences, HP-gas lung imaging allows not only static imaging of the lung lobes but also dynamic imaging of the trachea and bronchi of the lung [72] and obtain images of the tracheal distribution with sub-millimeter resolution [74]. Albert et al. evaluated HP-gas tracheal imaging and demonstrated that the bronchial diameters calculated using two different HP-gas imaging modalities for human class 0–5 bronchi were consistent with the classical Weibel model [75] (Fig. 9). Driehuys et al. examined healthy and partially fibrotic rats using ^{129}Xe imaging and found the significant restriction of ventilation in the lesioned portion [76].

The longitudinal relaxation time T1 of HP-gas decreased sharply with increasing paramagnetic oxygen concentration in the gas [77]. After entering the lung, HP-gas mixed with oxygen remaining in the alveoli, and in areas of high oxygen concentration, the T1 of HP-gas became shorter and weaker and appeared as a low signal on ventilation imaging, so that HP-gas lung ventilation MRI can reflect the distribution of oxygen concentration. The changes in oxygen concentration in the alveoli were caused by gas exchange and ventilation in the alveoli, which can reflect lesions caused by the gas exchange in

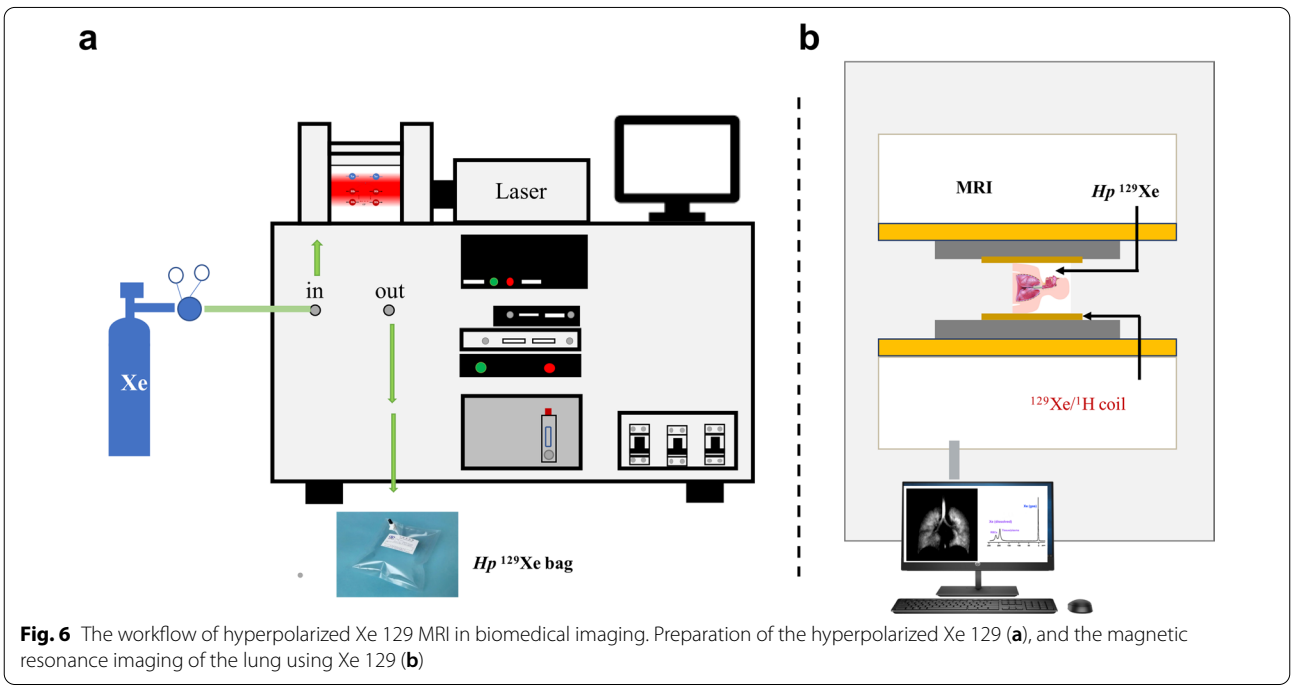

Fig. 6 The workflow of hyperpolarized Xe 129 MRI in biomedical imaging. Preparation of the hyperpolarized Xe 129 (**a**), and the magnetic resonance imaging of the lung using Xe 129 (**b**)

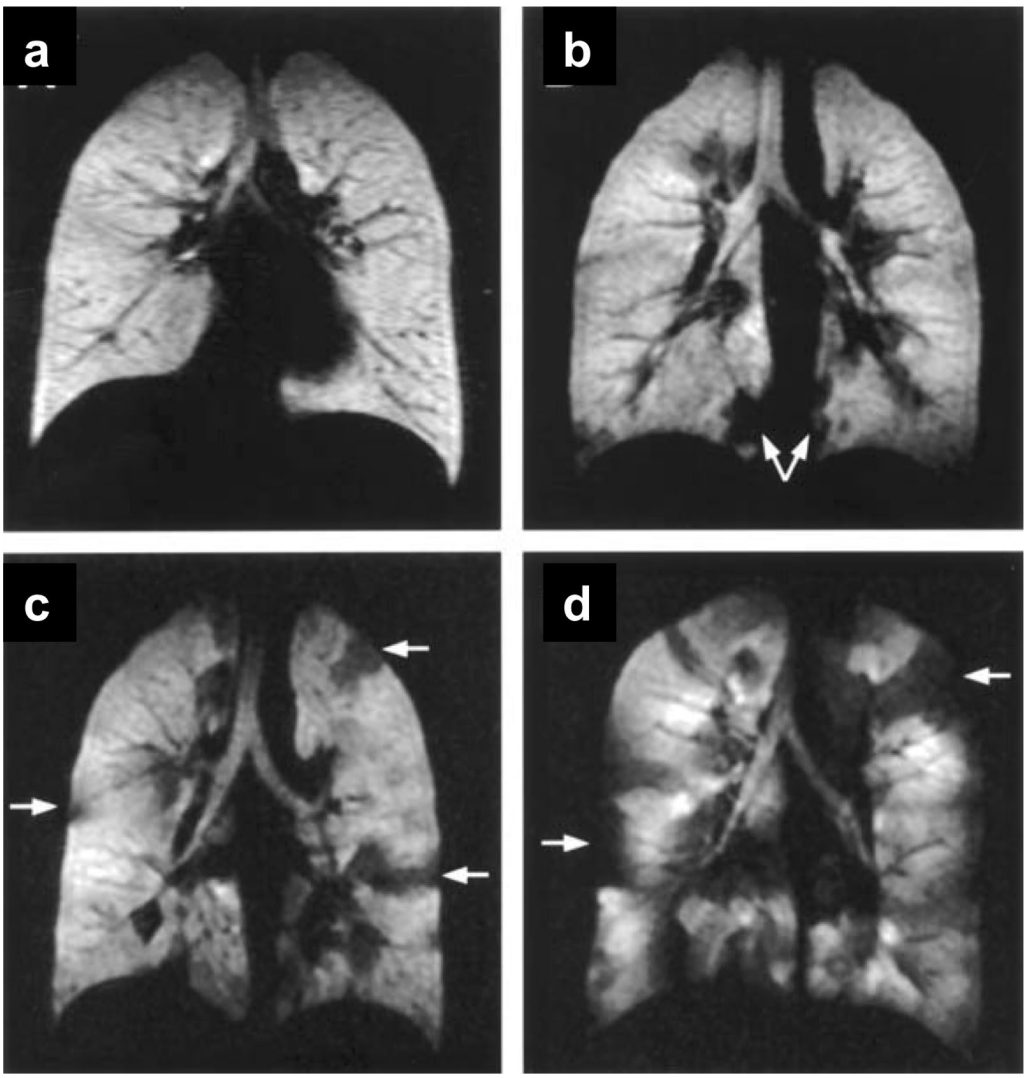

Fig. 7 Coronal MR images obtained immediately after inhalation of hyperpolarized Helium-3 gas in a healthy normal volunteer (**a**) and in patients with mild (FEV1 of 132% of predicted value. **b** Moderate (FEV1 of 83% of predicted value. **c** Severe (FEV1 of 34% of predicted value. **d** Asthma. The distribution of the gas is homogenous in the normal volunteer, and ventilation defects are seen with increasing numbers in the asthmatic patients with increasing severity (arrows pointing at several defects). Reproduced with permission from Elsevier Ltd (License Number: 5324281420540). J Allergy Clin Immunol. 2003 Jun;111(6):1205–11

the lungs [78–81], such as chronic obstructive pulmonary disease and COVID-19 [82, 83].

The apparent diffusion coefficient (ADC) distribution of HP-gas in the lung can reflect the local structural information of the lung, which in turn can reflect the gas diffusion function in the alveoli and enable the detection of lung diseases. For example, in patients with emphysema, the alveoli became larger, and the restriction of gas movement was reduced, resulting in an increase in the ADC value of the gas in the emphysematous region [70, 84–86]. A three-channel system (^{1}H, ^{3}He, and ^{129}Xe) could be used to simultaneously measure the diffusion coefficients of ^{3}He and ^{129}Xe, giving information on lung structure at different scales in a single sample [87]. In addition to the detection of lung structures, HP-gas ventilation imaging can also contribute to the diagnosis of lung cancer. Branca et al. achieved targeted detection of lung tumors by adding a superparamagnetic nanoparticle contrast agent that targets the lung tumor, affecting the homogeneity of the magnetic field in the targeted region through the superparamagnetic contrast agent, thereby altering T2* signal [88].

HP-gas MRI is non-radioactive and noninvasive and has great potential for the diagnosis and treatment

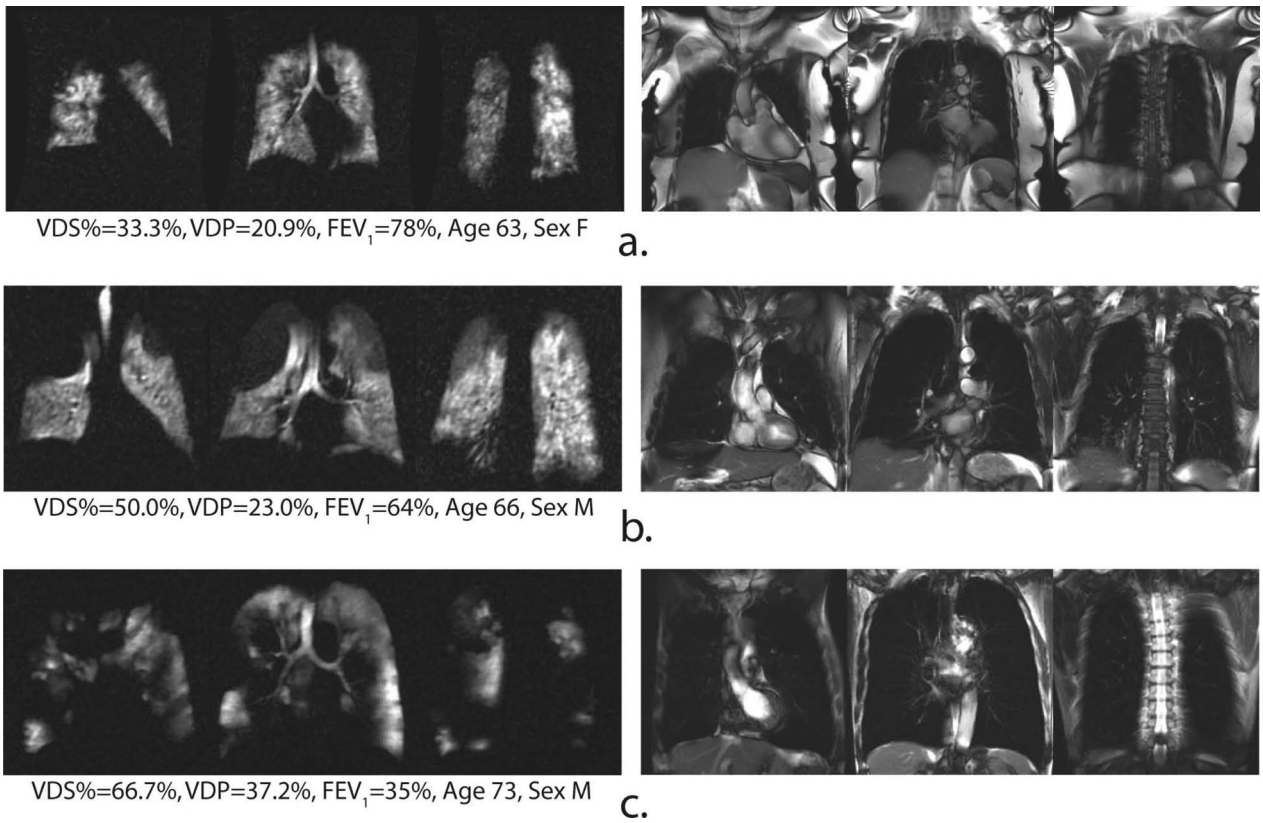

Fig. 8 Representative 129Xe ventilation (left) and 1H SSFP anatomical image (right) slices of three COPD subjects. Note, a variety of ventilation defects score percentage (VDS%) are observed increasingly from 33.3% (**a**), 50.0% (**b**) to 66.7% (**c**) throughout the lungs. SSFP; Steady-state Free Precession. Reproduced with permission from John Wiley and Sons (License Number: 5324291003853). NMR Biomed. 2013 April; 26(4): 424–435

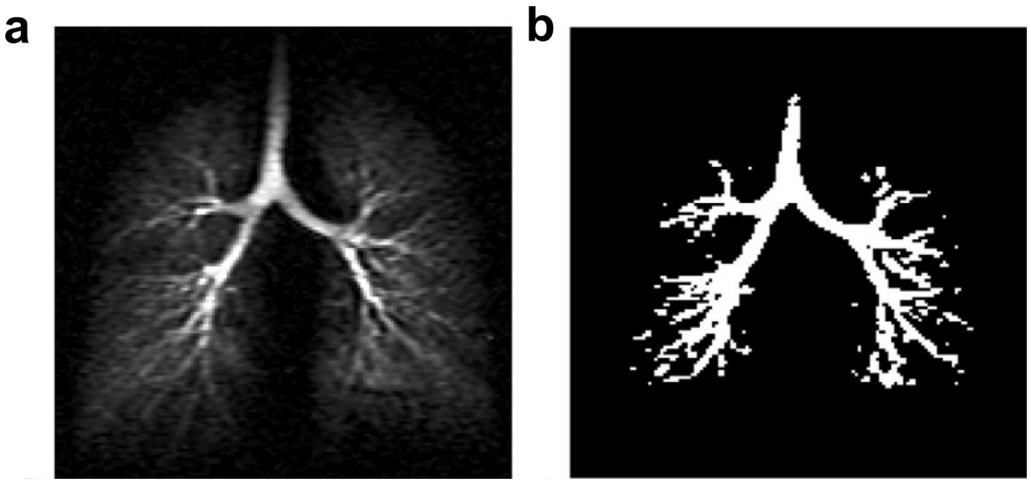

Fig. 9 Representative dynamic coronal MR images using hyperpolarized 3He MRI. Thresholding a dynamic projection image. **a** Before thresholding; **b** After thresholding. Reproduced with permission from John Wiley and Sons (License Number: 532430065345). Reproduced with permission from John Wiley and Sons (License Number: 5324291003853). NMR Biomed. 2013 April; 26(4): 424–435

of lung diseases, attracting great interest from many researchers. Although the spinning ratio of ^{129}Xe is only one-third of that of ^{3}He, resulting in a low MR sensitivity, the wide availability, and high natural abundance of ^{129}Xe compared with the extremely scarce resources of ^{3}He bring opportunities for the application of ^{129}Xe MRI, especially the good lipid solubility and chemical shift sensitivity of ^{129}Xe, which makes it unique for the detection of lung gas exchange function and has great potential for the early detection of lung diseases. It has great potential for the early detection of lung diseases. However, the HP-^{129}Xe MRI signal sensitivity needs to be further improved to obtain higher resolution lung images and more accurate lung function information, which requires innovative methods, techniques, and instruments for generating HP-gas, optimization of HP-gas delivery systems to reduce the loss of polarization, design of new imaging coils to utilize polarization more effectively, and development of new imaging pulse sequences to obtain more functional lung information. The development of new imaging pulse sequences to obtain more functional information about the lung. Cross-innovation with clinical medicine and biochemistry is also needed for better development and application of this technology.

Heart disease and diabetes

Phosphorus-31 is primarily used to study cell membrane phospholipid metabolism concerning ATP energy metabolism. By analyzing the concentration of phosphorus-containing metabolites in the tissue, the pH of the tissue can be obtained as well as determining the concentration of magnesium ions in the tissue [89]. ^{31}P MRS can be used to measure the myocardial high-energy phosphates phosphocreatine and ATP and to determine the ratio of phosphocreatine to ATP. Calculation of the ratio has been useful in identifying ischemia in animals [90, 91] and humans with coronary stenosis [89, 92–95].

Up to 40% of myocardial oxidative energy is derived from glucose and lactate in the blood, through which pyruvate is produced and enters the tricarboxylic acid cycle. HP-[1-^{13}C]-pyruvate has been shown to assess cardiac PDH levels and fluxes in vitro and in vivo to provide important information on myocardial activity [96, 97]. Currently, HP MRS is mostly used to assess metabolic changes in diseases such as myocardial infarction, heart failure, cardiac hypertrophy, and cardiac tumors [98, 99] (Fig. 10).

Dodd et al. applied HP-[1-^{13}C]-pyruvate and HP-[2-^{13}C]-pyruvate to assess changes in mitochondrial metabolism after myocardial infarction in rats [97]. The level of acetyl coenzyme A produced via PDH at week 6 post-infarction was normal, but its oxidation was reduced (slowing of the tricarboxylic acid cycle). At week 22 post-infarction, PDH levels were found to correlate significantly with cardiac ejection fraction, and both acetyl coenzyme A production and its oxidation were reduced. This predicts that HP MRSI has important research value in the assessment of cardiac metabolism. The literature reported that HP-[1-^{13}C]-pyruvate detected a significant decrease in [1-^{13}C]-alanine and [1-^{13}C]-lactate signals in the ischemia–reperfusion region of the left anterior descending coronary artery after 30 min of the blockade in a model of myocardial infarction, which was associated with cellular damage due to decreased cellular metabolism after severe myocardial hypoxia [100]. The HP-[1-^{13}C]-pyruvate MRSI was used to determine the changes of pyruvate metabolism in the heart and liver of rats treated with metformin, and the ratio of [1-^{13}C]-lactate to [1-^{13}C]-pyruvate in the heart and liver increased from 0.10 to 0.27 ($p=0.02$) and from 0.36 to 0.87 ($p=0.02$), respectively, demonstrating that HP-[1-^{13}C]-pyruvate MRSI can detect metformin-induced changes in cellular redox biology [101].

Diabetic nephropathy is one of the late complications of diabetes mellitus and one of the main causes of advanced renal failure. However, its pathogenesis remains not fully understood, and hypoxia in intrarenal tissues due to disturbances in oxygen metabolism is thought to be an important cause [102]. Laustsen C et al. used HP-[1-^{13}C]-pyruvate MRI to observe alterations in renal metabolism in early-type I diabetes and found that the [1-^{13}C]-lactate-to-[1-^{13}C]-pyruvate ratio was significantly elevated in diabetic kidneys, whereas the [1-^{13}C]-bicarbonate to [1-^{13}C]-pyruvate ratio was unchanged, renal oxygen consumption was increased, and the effective oxygen consumption rate was reduced [103]. Under different oxygen concentration conditions, the metabolism of [1-^{13}C]-pyruvate-to-lactate and alanine conversion in diabetic kidneys increased during acute hypoxia but did not alter bicarbonate flux, whereas lactate levels were normal at high oxygen concentrations [104]. This may explain why there is more nephropathy in diabetic patients living at high altitude [105]. Irregular insulin therapy increased the burden on the kidneys, which increased the uptake of [1-^{13}C]-pyruvate and simultaneously increase the metabolic fluxes of anaerobic and aerobic metabolism (elevated lactate, alanine, and bicarbonate signals), leading to increased consumption of energy substances [106]. This suggests that strict glycemic control is important in insulin-dependent diabetes and that disturbances in renal metabolism in poor glycemic control are dependent on the consumption of energy substrates, which may herald new therapeutic targets for diabetic nephropathy.

In insulin-resistant type II diabetes, excessive hepatic gluconeogenesis and glycogenolysis can cause a rise in blood glucose, and HP-[1-^{13}C]-pyruvate MRSI allowed

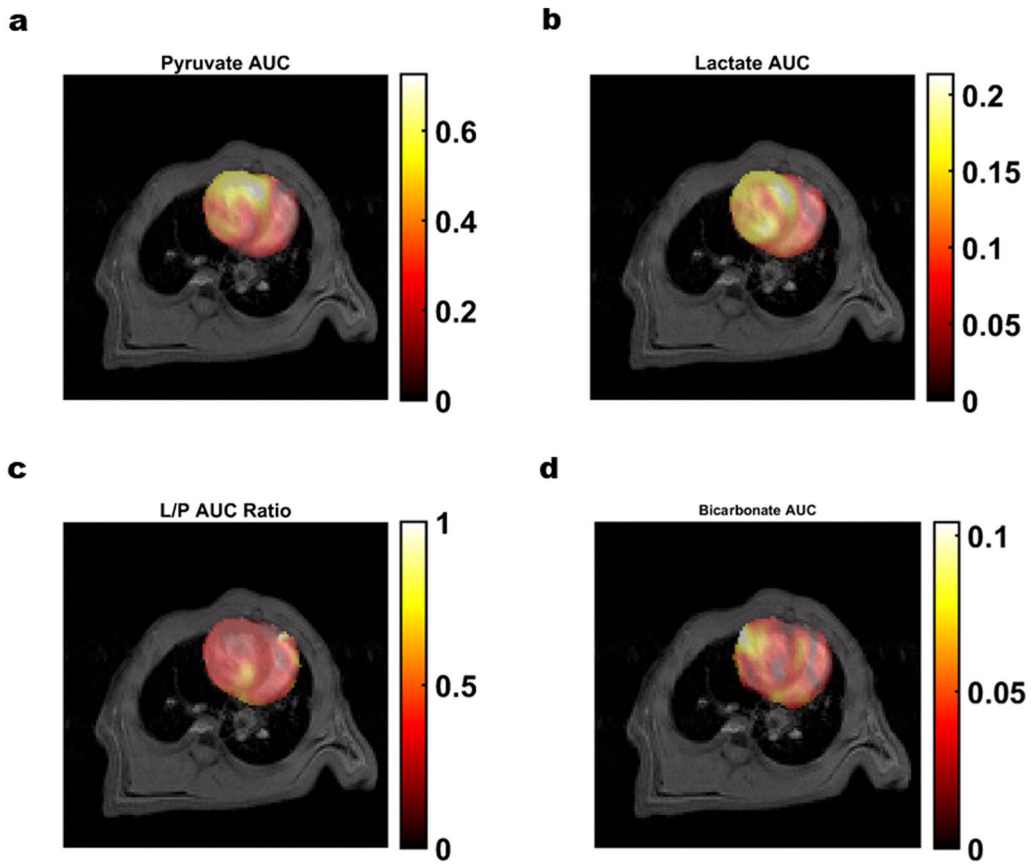

Fig. 10 ^{13}C images of pyruvate (**a**), lactate (**b**), lactate/pyruvate (L/P) area under the curve (AUC) ratio (**c**), and bicarbonate (**d**) in the LV measured using dynamic HP [1-13C]pyruvate MRI. Metabolite images (color) are overlaid on T1-weighted axial images (grayscale) for anatomical reference. Reproduced with permission from Elsevier Ltd (License Number: 5324651196851). Magn Reson Imaging. 2020 May;68:9–17

noninvasive dynamic real-time measurement of hepatic metabolic alterations in vivo [52]. The livers of diabetic mice exhibit higher signals of ^{13}C-oxaloacetate, ^{13}C-aspartate, and ^{13}C-malate, compared to normal mice injected with glucagon gluconeogenesis was increased similarly. Two weeks after metformin treatment, hepatic gluconeogenesis was reduced, ^{13}C-aspartate and ^{13}C-malate and the amount of ^{13}C-labeled aspartate and malate decreased, the conversion of pyruvate to aspartate and malate also decreased, and blood glucose levels decreased, which is consistent with a downregulation of gluconeogenesis. The [1-^{13}C]-pyruvate can be used as a biomarker to diagnose liver dysfunction in diabetes and to help assess treatment. The successful use of HP-^{13}C metabolic imaging in diabetic disease models has a positive impact on the mechanism, treatment, and management of clinical diabetes itself and its complications.

Challenges and future opportunities

NMR spectroscopy is the only non-radiation tool that provides the opportunity to insight the molecular metabolically changes in vivo and provides detailed structural information for molecules. NMR is thus important in real-time imaging of metabolic activities not only for biochemists but also for the clinical scientists. The exploration of the detected metabolic signals with high sensitivity, efficiency, and stability is the external pursuit for the realization of practically, clinical usefully NMR spectroscopy imaging, and this always remains the challenges. To improve the sensitivity of the NMR spectroscopy and overcome the challenges, four major directions are pushed to increase the detection sensitivity of NMR spectroscopy.

Firstly, higher magnetic fields. The sensitivity of NMR spectroscopy increases with the higher magnetic fields, and the signal of the routine used ^{1}H as well as the less sensitivity nucleus such as ^{2}H, ^{13}C, ^{15} N, ^{31}P, ^{18}F, and ^{23}Na will be greatly boosted with the increased magnetic fields, which provides a potential direction despite many practical difficulties. At present, many higher magnetic fields strength have been used clinically or scientifically, the cutting edge of the clinically available higher magnetic

fields is 7.0 T and 9.4 T in human [107, 108], and even the much more higher 11.7 T is potentially available [109]. However, the expensive cost, massive use of liquid helium, and huge site requirements limit its transition from dedicated laboratories to widespread clinical use, and innovative design and application of newly superconducting materials may breakthrough the dilemma.

Secondly, development of high sensitivity NMR coils. Another very important strategy is to increase the signal sensitivity by developing higher sensitivity NMR coils. With the development of new materials and innovative design, more elements can be synthesized into the coil with higher density. In addition, the coil can be also designed more closely fitted with the surface of human body that means shorter coil-to-sample distance and which can also help further improve the signal sensitivity. The air coil may represent this new direction [110]. Besides, commercially available dual-tuned (^{1}H and 13C) multichannel coils that allow high signal-to-noise ratio imaging for all body areas are essential [2].

Thirdly, using hyperpolarization to improve the signal sensitivity. Dynamic nuclear polarization technique has been emerged as a powerful molecular strategy which allows safe, non-radiation injury, real-time, and metabolic-specific investigation of the dynamic metabolic process. Hyperpolarized MRI of ^{13}C-labeled compounds have been shown to increase the signal sensitivity more than 10,000-fold [2]; this offers great potential to trace specific metabolic process in various lesions. However, its main limitation is that the current hyperpolarization technique can be only applicable to few molecular. Generation and co-hyperpolarization of multiple molecules provide the potential to make large number of molecules to be hyperpolarized and simultaneously insight the multiple metabolic pathways. Additionally, the other limitation of the HP techniques is that the produced HP substances or HP contrast agents generally cannot be re-hyperpolarized after their administration, and the hard-won HP state will exponentially decay back to the equilibrium. This decay ostensibly poses a fundamental limit on the time scale of biochemical processes that can be probed by HP contrast agents and requires HP lifetimes that are sufficiently log (> ten of seconds) for agent manipulation after its production, administration (e.g., inhalation or injection), in vivo delivery, and observation of metabolic and functional event [111]. Thus, innovative polarization approaches should be developed to overcome the limitations of shorter hyperpolarized signal lasts time and relatively sophisticated hyperpolarization technique in the produce and probe delivery.

Last but not least, ultra-fast MR imaging sequences and innovative parsing algorithm [112]. To develop ultra-fast MR imaging sequences is another promising approach to increase the signal sensitivity. As mentioned above, the hyperpolarized signal only lasts for few minutes; thus, maximizing signal acquisition in a limited time can further increase the signal sensitivity. In addition, using innovative parsing algorithm to separate the acquired signal and to further strength the target signal may also contribute to the signal improvement.

Conclusions

Multi-nuclear magnetic resonance spectroscopy is an emerging technique. With the development of magnetic resonance software and hardware, multi-nuclear magnetic resonance imaging has been applied to the basic and clinical transformation of various systems of human. Its unique advantages for displaying the real-time, dynamic metabolic process in different pathological processes provide the possibility for early diagnosis, evaluation of therapeutic efficacy, decision-making, drug development, and even exploration of new disease mechanisms. Despite these achievements, there is much progress yet to be made. Innovation of the polarization technique, exploration of new probes, quantification, and standardization of the results and construction of more prospective multicenter trials can further promote the clinical transformation of the advanced NMR technique.

Abbreviations

^{18}F-FDG: ^{18}F-fluorodeoxyglucose; AS: Alport syndrome; BBB: Blood–brain barrier; HP: Hyperpolarization; LDH: Lactate dehydrogenase; MCT: Monocarboxylate transporter; MP: Mononuclear phagocyte; MRI: Magnetic resonance imaging; MRSI: Magnetic resonance spectroscopic imaging; MS: Multiple sclerosis; NMR: Nuclear magnetic resonance; PDH: Pyruvate dehydrogenase; PET: Positron emission tomography; RCC: Renal cell carcinoma; TBI: Traumatic brain injury.

Author contributions

YW, QL, FC, and C-WY collected materials and the literature. F-F G, TZ, SW, and C-WY organized the literature and extracted data. C-WY, YW, and J-Z W wrote the manuscript. YW, H-Y J, and BS revised the manuscript. All authors read and approved the final manuscript.

Funding

This work was supported by Science and Technology Support Program of Sichuan Province (Grant number 2021YFS0144, Grant number 2021YFS0021), China Postdoctoral Science Foundation (2021M692289), Post-Doctor Research Project, West China Hospital, Sichuan University (Grant number 2020HXBH130).

Availability of data and materials

The data and material are included in this manuscript.

Declarations

Ethics approval and consent to participate

The authors are accountable for all aspects of the work in ensuring that questions related to the accuracy or integrity of any part of the work are appropriately investigated and resolved.

Consent for publication
All authors and all patients involved are agreed to the publication of this manuscript.

Competing interests
The authors have no conflicts of interest to declare.

Author details
[1]Department of Radiology, West China Hospital, Sichuan University, No. 37, Guoxue Alley, Chengdu 610041, People's Republic of China. [2]Clinical & Technical Support, Philips Healthcare, Beijing, China. [3]Department of Radiology, Sanya People's Hospital, Sanya, China.

Received: 10 March 2022 Accepted: 4 July 2022
Published online: 17 August 2022

References

1. Edelman RR (2014) The history of MR imaging as seen through the pages of radiology. Radiology 273:S181-200
2. Wang ZJ, Ohliger MA, Larson PEZ et al (2019) Hyperpolarized (13)C MRI: state of the art and future directions. Radiology 291:273–284
3. Stewart NJ, Matsumoto S (2021) Biomedical applications of the dynamic nuclear polarization and parahydrogen induced polarization techniques for hyperpolarized (13)C MR imaging. Magn Reson Med Sci 20:1–17
4. Adamson EB, Ludwig KD, Mummy DG, Fain SB (2017) Magnetic resonance imaging with hyperpolarized agents: methods and applications. Phys Med Biol 62:R81-r123
5. Jacobs MA, Stearns V, Wolff AC et al (2010) Multiparametric magnetic resonance imaging, spectroscopy and multinuclear (23Na) imaging monitoring of preoperative chemotherapy for locally advanced breast cancer. Acad Radiol 17:1477–1485
6. Le Page LM, Guglielmetti C, Taglang C, Chaumeil MM (2020) Imaging brain metabolism using hyperpolarized (13)C magnetic resonance spectroscopy. Trends Neurosci 43:343–354
7. Grist JT, Miller JJ, Zaccagna F et al (2020) Hyperpolarized (13)C MRI: a novel approach for probing cerebral metabolism in health and neurological disease. J Cereb Blood Flow Metab 40:1137–1147
8. Hurd RE, Yen YF, Chen A, Ardenkjaer-Larsen JH (2012) Hyperpolarized 13C metabolic imaging using dissolution dynamic nuclear polarization. J Magn Reson Imaging 36:1314–1328
9. Kettenmann H, Hanisch UK, Noda M, Verkhratsky A (2011) Physiology of microglia. Physiol Rev 91:461–553
10. Tannahill GM, Iraci N, Gaude E, Frezza C, Pluchino S (2015) Metabolic reprograming of mononuclear phagocytes in progressive multiple sclerosis. Front Immunol 6:106
11. Kelly B, O'Neill LA (2015) Metabolic reprogramming in macrophages and dendritic cells in innate immunity. Cell Res 25:771–784
12. Guglielmetti C, Najac C, Didonna A, Van der Linden A, Ronen SM, Chaumeil MM (2017) Hyperpolarized (13)C MR metabolic imaging can detect neuroinflammation in vivo in a multiple sclerosis murine model. Proc Natl Acad Sci U S A 114:E6982-e6991
13. Carpenter KL, Jalloh I, Gallagher CN et al (2014) (13)C-labelled microdialysis studies of cerebral metabolism in TBI patients. Eur J Pharm Sci 57:87–97
14. Robertson CL, Saraswati M, Fiskum G (2007) Mitochondrial dysfunction early after traumatic brain injury in immature rats. J Neurochem 101:1248–1257
15. Guglielmetti C, Chou A, Krukowski K et al (2017) In vivo metabolic imaging of traumatic brain injury. Sci Rep 7:17525
16. DeVience SJ, Lu X, Proctor J et al (2017) Metabolic imaging of energy metabolism in traumatic brain injury using hyperpolarized [1-(13)C] pyruvate. Sci Rep 7:1907
17. Hackett EP, Pinho MC, Harrison CE et al (2020) Imaging acute metabolic changes in patients with mild traumatic brain injury using hyperpolarized [1-(13)C]pyruvate. iScience 23:101885
18. Grist JT, McLean MA, Riemer F et al (2019) Quantifying normal human brain metabolism using hyperpolarized [1-(13)C]pyruvate and magnetic resonance imaging. Neuroimage 189:171–179
19. Xu Y, Ringgaard S, Mariager C et al (2017) Hyperpolarized (13)C magnetic resonance imaging can detect metabolic changes characteristic of penumbra in ischemic stroke. Tomography 3:67–73
20. Zhou X, Sun Y, Mazzanti M et al (2011) MRI of stroke using hyperpolarized 129Xe. NMR Biomed 24:170–175
21. De Feyter HM, Behar KL, Corbin ZA et al (2018) Deuterium metabolic imaging (DMI) for MRI-based 3D mapping of metabolism in vivo. Sci Adv 4:eaat7314
22. Hesse F, Somai V, Kreis F, Bulat F, Wright AJ, Brindle KM (2021) Monitoring tumor cell death in murine tumor models using deuterium magnetic resonance spectroscopy and spectroscopic imaging. Proc Natl Acad Sci U S A. https://doi.org/10.1073/pnas.2014631118
23. Kreis F, Wright AJ, Hesse F, Fala M, Hu DE, Brindle KM (2020) Measuring tumor glycolytic flux in vivo by using fast deuterium MRI. Radiology 294:289–296
24. Park I, Larson PEZ, Zierhut ML et al (2010) Hyperpolarized C-13 magnetic resonance metabolic imaging: application to brain tumors. Neuro Oncol 12:133–144
25. Hurd RE, Yen YF, Mayer D et al (2010) Metabolic imaging in the anesthetized rat brain using hyperpolarized 1-C-13 pyruvate and 1-C-13 ethyl pyruvate. Magn Reson Med 63:1137–1143
26. Park I, Larson PEZ, Gordon JW et al (2018) Development of methods and feasibility of using hyperpolarized carbon-13 imaging data for evaluating brain metabolism in patient studies. Magn Reson Med 80:864–873
27. Miloushev VZ, Granlund KL, Boltyanskiy R et al (2018) Metabolic imaging of the human brain with hyperpolarized (13)C pyruvate demonstrates (13)C lactate production in brain tumor patients. Cancer Res 78:3755–3760
28. Day SE, Kettunen MI, Cherukuri MK et al (2011) Detecting response of rat C6 glioma tumors to radiotherapy using hyperpolarized [1- 13C] pyruvate and 13C magnetic resonance spectroscopic imaging. Magn Reson Med 65:557–563
29. Ward CS, Venkatesh HS, Chaumeil MM et al (2010) Noninvasive detection of target modulation following phosphatidylinositol 3-kinase inhibition using hyperpolarized 13C magnetic resonance spectroscopy. Cancer Res 70:1296–1305
30. Choi SY, Xue H, Wu R et al (2016) The MCT4 gene: a novel, potential target for therapy of advanced prostate cancer. Clin Cancer Res 22:2721–2733
31. Granlund KL, Tee SS, Vargas HA et al (2020) Hyperpolarized MRI of human prostate cancer reveals increased lactate with tumor grade driven by monocarboxylate transporter 1. Cell Metab 31:105-114. e103
32. Keshari KR, Sriram R, Koelsch BL et al (2013) Hyperpolarized 13C-pyruvate magnetic resonance reveals rapid lactate export in metastatic renal cell carcinomas. Cancer Res 73:529–538
33. Sriram R, Van Criekinge M, Hansen A et al (2015) Real-time measurement of hyperpolarized lactate production and efflux as a biomarker of tumor aggressiveness in an MR compatible 3D cell culture bioreactor. NMR Biomed 28:1141–1149
34. Sriram R, Van Criekinge M, DeLos SJ et al (2016) Non-invasive differentiation of benign renal tumors from clear cell renal cell carcinomas using clinically translatable hyperpolarized (13)C pyruvate magnetic resonance. Tomography 2:35–42
35. Sriram R, Gordon J, Baligand C et al (2018) Non-invasive assessment of lactate production and compartmentalization in renal cell carcinomas using hyperpolarized (13)C pyruvate MRI. Cancers (Basel) 10
36. Nelson SJ, Kurhanewicz J, Vigneron DB et al (2013) Metabolic imaging of patients with prostate cancer using hyperpolarized [1–13C] pyruvate. Sci Transl Med 5:198ra108
37. Sushentsev N, McLean MA, Warren AY et al (2022) Hyperpolarised (13)C-MRI identifies the emergence of a glycolytic cell population within intermediate-risk human prostate cancer. Nat Commun 13:466
38. Albers MJ, Bok R, Chen AP et al (2008) Hyperpolarized 13C lactate, pyruvate, and alanine: noninvasive biomarkers for prostate cancer detection and grading. Cancer Res 68:8607–8615
39. Day SE, Kettunen MI, Gallagher FA et al (2007) Detecting tumor response to treatment using hyperpolarized 13C magnetic resonance imaging and spectroscopy. Nat Med 13:1382–1387

40. Dafni H, Larson PE, Hu S et al (2010) Hyperpolarized 13C spectroscopic imaging informs on hypoxia-inducible factor-1 and myc activity downstream of platelet-derived growth factor receptor. Cancer Res 70:7400–7410
41. Zierhut ML, Yen YF, Chen AP et al (2010) Kinetic modeling of hyperpolarized 13C1-pyruvate metabolism in normal rats and TRAMP mice. J Magn Reson 202:85–92
42. Kanamaru H, Oyama N, Akino H, Okada K (2000) Evaluation of prostate cancer using FDG-PET. Hinyokika Kiyo 46:851–853
43. Baligand C, Qin H, True-Yasaki A et al (2017) Hyperpolarized (13) C magnetic resonance evaluation of renal ischemia reperfusion injury in a murine model. NMR Biomed 30
44. Moon CM, Oh CH, Ahn KY et al (2017) Metabolic biomarkers for non-alcoholic fatty liver disease induced by high-fat diet: In vivo magnetic resonance spectroscopy of hyperpolarized [1-(13)C] pyruvate. Biochem Biophys Res Commun 482:112–119
45. Moon CM, Shin SS, Lim NY et al (2018) Metabolic alterations in a rat model of hepatic ischaemia reperfusion injury: in vivo hyperpolarized (13) C MRS and metabolic imaging. Liver Int 38:1117–1127
46. Josan S, Billingsley K, Orduna J et al (2015) Assessing inflammatory liver injury in an acute CCl4 model using dynamic 3D metabolic imaging of hyperpolarized [1-(13)C]pyruvate. NMR Biomed 28:1671–1677
47. Moreno KX, Satapati S, DeBerardinis RJ, Burgess SC, Malloy CR, Merritt ME (2014) Real-time detection of hepatic gluconeogenic and glycogenolytic states using hyperpolarized [2-13C]dihydroxyacetone. J Biol Chem 289:35859–35867
48. Wilson DM, Di Gialleonardo V, Wang ZJ et al (2017) Hyperpolarized (13)C spectroscopic evaluation of oxidative stress in a rodent model of steatohepatitis. Sci Rep 7:46014
49. Kim GW, Ahn KY, Kim YH, Jeong GW (2016) Time-course metabolic changes in high-fat diet-induced obesity rats: a pilot study using hyperpolarized (13)C dynamic MRS. Magn Reson Imaging 34:1199–1205
50. Can E, Bastiaansen JAM, Couturier DL, Gruetter R, Yoshihara HAI, Comment A (2022) [(13)C]bicarbonate labelled from hyperpolarized [1-(13) C]pyruvate is an in vivo marker of hepatic gluconeogenesis in fasted state. Commun Biol 5:10
51. Chen J, Hackett EP, Kovacs Z, Malloy CR, Park JM (2021) Assessment of hepatic pyruvate carboxylase activity using hyperpolarized [1-(13) C]-l-lactate. Magn Reson Med 85:1175–1182
52. Lee P, Leong W, Tan T, Lim M, Han W, Radda GK (2013) In vivo hyperpolarized carbon-13 magnetic resonance spectroscopy reveals increased pyruvate carboxylase flux in an insulin-resistant mouse model. Hepatology 57:515–524
53. Wang JX, Merritt ME, Sherry D, Malloy CR (2016) A general chemical shift decomposition method for hyperpolarized (13) C metabolite magnetic resonance imaging. Magn Reson Chem 54:665–673
54. Smith LM, Pitts CB, Friesen-Waldner LJ et al (2021) In vivo magnetic resonance spectroscopy of hyperpolarized [1-(13) C]pyruvate and proton density fat fraction in a guinea pig model of non-alcoholic fatty liver disease development after life-long western diet consumption. J Magn Reson Imaging 54:1404–1414
55. Yoshimitsu K (2014) Transarterial chemoembolization using iodized oil for unresectable hepatocellular carcinoma: perspective from multistep hepatocarcinogenesis. Hepat Med 6:89–94
56. Park YN, Kim MJ (2011) Hepatocarcinogenesis: imaging-pathologic correlation. Abdom Imaging 36:232–243
57. Hu S, Balakrishnan A, Bok RA et al (2011) 13C-pyruvate imaging reveals alterations in glycolysis that precede c-Myc-induced tumor formation and regression. Cell Metab 14:131–142
58. Gallagher FA, Kettunen MI, Day SE, Lerche M, Brindle KM (2008) 13C MR spectroscopy measurements of glutaminase activity in human hepatocellular carcinoma cells using hyperpolarized 13C-labeled glutamine. Magn Reson Med 60:253–257
59. von Morze C, Larson PE, Hu S et al (2011) Imaging of blood flow using hyperpolarized [(13)C]urea in preclinical cancer models. J Magn Reson Imaging 33:692–697
60. Bliemsrieder E, Kaissis G, Grashei M et al (2021) Hyperpolarized (13) C pyruvate magnetic resonance spectroscopy for in vivo metabolic phenotyping of rat HCC. Sci Rep 11:1191
61. Kveder M, Zupancic I, Lahajnar G et al (1988) Water proton NMR relaxation mechanisms in lung tissue. Magn Reson Med 7:432–441
62. Togao O, Tsuji R, Ohno Y, Dimitrov I, Takahashi M (2010) Ultrashort echo time (UTE) MRI of the lung: assessment of tissue density in the lung parenchyma. Magn Reson Med 64:1491–1498
63. Walker TG, Happer W (1997) Spin-exchange optical pumping of noble-gas nuclei. Rev Mod Phys 69:629–642. https://doi.org/10.1103/revmodphys.69.629
64. Hughes-Riley T, Six JS, Lilburn DML et al (2013) Cryogenics free production of hyperpolarized 129Xe and 83Kr for biomedical MRI applications. J Magn Reson 237:23–33
65. Pavlovskaya GE, Cleveland ZI, Stupic KF, Basaraba RJ, Meersmann T (2005) Hyperpolarized krypton-83 as a contrast agent for magnetic resonance imaging. Proc Natl Acad Sci U S A 102:18275–18279
66. Six JS, Hughes-Riley T, Lilburn DM et al (2014) Pulmonary MRI contrast using surface quadrupolar relaxation (SQUARE) of hyperpolarized (83) Kr. Magn Reson Imaging 32:48–53
67. Couch MJ, Fox MS, Viel C et al (2016) Fractional ventilation mapping using inert fluorinated gas MRI in rat models of inflammation and fibrosis. NMR Biomed 29:545–552
68. Gutberlet M, Kaireit TF, Voskrebenzev A et al (2018) Free-breathing dynamic (19)F gas MR imaging for mapping of regional lung ventilation in patients with COPD. Radiology 286:1040–1051
69. Mathew L, Evans A, Ouriadov A et al (2008) Hyperpolarized 3He magnetic resonance imaging of chronic obstructive pulmonary disease: reproducibility at 3.0 tesla. Acad Radiol 15:1298–1311
70. de Lange EE, Altes TA, Patrie JT et al (2006) Evaluation of asthma with hyperpolarized helium-3 MRI: correlation with clinical severity and spirometry. Chest 130:1055–1062
71. Woodhouse N, Wild JM, Paley MN et al (2005) Combined helium-3/proton magnetic resonance imaging measurement of ventilated lung volumes in smokers compared to never-smokers. J Magn Reson Imaging 21:365–369
72. Virgincar RS, Cleveland ZI, Kaushik SS et al (2013) Quantitative analysis of hyperpolarized 129Xe ventilation imaging in healthy volunteers and subjects with chronic obstructive pulmonary disease. NMR Biomed 26:424–435
73. Samee S, Altes T, Powers P et al (2003) Imaging the lungs in asthmatic patients by using hyperpolarized helium-3 magnetic resonance: assessment of response to methacholine and exercise challenge. J Allergy Clin Immunol 111:1205–1211
74. Johnson GA, Cofer GP, Hedlund LW, Maronpot RR, Suddarth SA (2001) Registered (1)H and (3)He magnetic resonance microscopy of the lung. Magn Reson Med 45:365–370
75. Lewis TA, Tzeng YS, McKinstry EL et al (2005) Quantification of airway diameters and 3D airway tree rendering from dynamic hyperpolarized 3He magnetic resonance imaging. Magn Reson Med 53:474–478
76. Driehuys B, Pollaro J, Cofer GP (2008) In vivo MRI using real-time production of hyperpolarized 129Xe. Magn Reson Med 60:14–20
77. Saam B, Happer W, Middleton H (1995) Nuclear relaxation of 3He in the presence of O2. Phys Rev A 52:862–865
78. Cieślar K, Stupar V, Canet-Soulas E, Gaillard S, Crémillieux Y (2007) Alveolar oxygen partial pressure and oxygen depletion rate mapping in rats using 3He ventilation imaging. Magn Reson Med 57:423–430
79. Cieślar K, Alsaid H, Stupar V et al (2007) Measurement of nonlinear pO2 decay in mouse lungs using 3He-MRI. NMR Biomed 20:383–391
80. Kadlecek S, Mongkolwisetwara P, Xin Y et al (2011) Regional determination of oxygen uptake in rodent lungs using hyperpolarized gas and an analytical treatment of intrapulmonary gas redistribution. NMR Biomed 24:1253–1263
81. Wild JM, Fichele S, Woodhouse N, Paley MN, Kasuboski L, van Beek EJ (2005) 3D volume-localized pO2 measurement in the human lung with 3He MRI. Magn Reson Med 53:1055–1064
82. Marshall H, Parra-Robles J, Deppe MH, Lipson DA, Lawson R, Wild JM (2014) (3)He pO2 mapping is limited by delayed-ventilation and diffusion in chronic obstructive pulmonary disease. Magn Reson Med 71:1172–1178
83. Li H, Zhao X, Wang Y et al (2021) Damaged lung gas exchange function of discharged COVID-19 patients detected by hyperpolarized (129)Xe MRI. Sci Adv. https://doi.org/10.1126/sciadv.abc8180

84. Kaushik SS, Cleveland ZI, Cofer GP et al (2011) Diffusion-weighted hyperpolarized 129Xe MRI in healthy volunteers and subjects with chronic obstructive pulmonary disease. Magn Reson Med 65:1154–1165
85. Saam BT, Yablonskiy DA, Kodibagkar VD et al (2000) MR imaging of diffusion of (3)He gas in healthy and diseased lungs. Magn Reson Med 44:174–179
86. Salerno M, Altes TA, Mugler JP 3rd, Nakatsu M, Hatabu H, de Lange EE (2001) Hyperpolarized noble gas MR imaging of the lung: potential clinical applications. Eur J Radiol 40:33–44
87. Wild JM, Marshall H, Xu X et al (2013) Simultaneous imaging of lung structure and function with triple-nuclear hybrid MR imaging. Radiology 267:251–255
88. Driehuys B, Cofer GP, Pollaro J, Mackel JB, Hedlund LW, Johnson GA (2006) Imaging alveolar-capillary gas transfer using hyperpolarized 129Xe MRI. Proc Natl Acad Sci U S A 103:18278–18283
89. Buchthal SD, den Hollander JA, Merz CN et al (2000) Abnormal myocardial phosphorus-31 nuclear magnetic resonance spectroscopy in women with chest pain but normal coronary angiograms. N Engl J Med 342:829–835
90. Schaefer S, Camacho SA, Gober J et al (1989) Response of myocardial metabolites to graded regional ischemia: 31P NMR spectroscopy of porcine myocardium in vivo. Circ Res 64:968–976
91. Schaefer S, Schwartz GG, Gober JR et al (1990) Relationship between myocardial metabolites and contractile abnormalities during graded regional ischemia. Phosphorus-31 nuclear magnetic resonance studies of porcine myocardium in vivo. J Clin Invest 85:706–713
92. Nunnally RL, Bottomley PA (1981) Assessment of pharmacological treatment of myocardial infarction by phosphorus-31 NMR with surface coils. Science 211:177–180
93. Flaherty JT, Weisfeldt ML, Bulkley BH, Gardner TJ, Gott VL, Jacobus WE (1982) Mechanisms of ischemic myocardial cell damage assessed by phosphorus-31 nuclear magnetic resonance. Circulation 65:561–570
94. Bottomley PA, Herfkens RJ, Smith LS, Bashore TM (1987) Altered phosphate metabolism in myocardial infarction: P-31 MR spectroscopy. Radiology 165:703–707
95. Neubauer S, Krahe T, Schindler R et al (1992) 31P magnetic resonance spectroscopy in dilated cardiomyopathy and coronary artery disease. altered cardiac high-energy phosphate metabolism in heart failure. Circulation 86:1810–1818
96. Malloy CR, Merritt ME, Sherry AD (2011) Could 13C MRI assist clinical decision-making for patients with heart disease? NMR Biomed 24:973–979
97. Dodd MS, Atherton HJ, Carr CA et al (2014) Impaired in vivo mitochondrial Krebs cycle activity after myocardial infarction assessed using hyperpolarized magnetic resonance spectroscopy. Circ Cardiovasc Imaging 7:895–904
98. Rider OJ, Tyler DJ (2013) Clinical implications of cardiac hyperpolarized magnetic resonance imaging. J Cardiovasc Magn Reson 15:93
99. Barton GP, Macdonald EB, Goss KN, Eldridge MW, Fain SB (2020) Measuring the link between cardiac mechanical function and metabolism during hyperpolarized (13)C-pyruvate magnetic resonance experiments. Magn Reson Imaging 68:9–17
100. Merritt ME, Harrison C, Storey C, Jeffrey FM, Sherry AD, Malloy CR (2007) Hyperpolarized 13C allows a direct measure of flux through a single enzyme-catalyzed step by NMR. Proc Natl Acad Sci U S A 104:19773–19777
101. Lewis AJ, Miller JJ, McCallum C et al (2016) Assessment of metformin-induced changes in cardiac and hepatic redox state using hyperpolarized[1-13C]pyruvate. Diabetes 65:3544–3551
102. Hansell P, Welch WJ, Blantz RC, Palm F (2013) Determinants of kidney oxygen consumption and their relationship to tissue oxygen tension in diabetes and hypertension. Clin Exp Pharmacol Physiol 40:123–137
103. Laustsen C, Ostergaard JA, Lauritzen MH et al (2013) Assessment of early diabetic renal changes with hyperpolarized 1–13C pyruvate. Diabetes Metab Res Rev 29:125–129
104. Laustsen C, Lycke S, Palm F et al (2014) High altitude may alter oxygen availability and renal metabolism in diabetics as measured by hyperpolarized 1-C-13 pyruvate magnetic resonance imaging. Kidney Int 86:67–74
105. Hochman ME, Watt JP, Reid R, O'Brien KL (2007) The prevalence and incidence of end-stage renal disease in native American adults on the Navajo reservation. Kidney Int 71:931–937
106. Laustsen C, Lipso K, Ostergaard JA et al (2014) Insufficient insulin administration to diabetic rats increases substrate utilization and maintains lactate production in the kidney. Physiol Rep. https://doi.org/10.14814/phy2.12233
107. Paech D, Nagel AM, Schultheiss MN et al (2020) Quantitative dynamic oxygen 17 MRI at 7.0 T for the cerebral oxygen metabolism in glioma. Radiology 295:181–189
108. Murali-Manohar S, Borbath T, Wright AM, Soher B, Mekle R, Henning A (2020) T(2) relaxation times of macromolecules and metabolites in the human brain at 9.4 T. Magn Reson Med 84:542–558
109. Tanoue M, Saito S, Takahashi Y et al (2019) Amide proton transfer imaging of glioblastoma, neuroblastoma, and breast cancer cells on a 11.7 T magnetic resonance imaging system. Magn Reson Imaging 62:181–190
110. Cogswell PM, Trzasko JD, Gray EM et al (2021) Application of adaptive image receive coil technology for whole-brain imaging. AJR Am J Roentgenol 216:552–559
111. Nikolaou P, Goodson BM, Chekmenev EY (2015) NMR hyperpolarization techniques for biomedicine. Chemistry 21:3156–3166
112. Feinberg DA, Setsompop K (2013) Ultra-fast MRI of the human brain with simultaneous multi-slice imaging. J Magn Reson 229:90–100

Publisher's Note